

Full length article

Sequential nucleation of phases in a 17-4PH steel: Microstructural characterisation and mechanical properties



Guma Yeli^a, Maria A. Auger^a, Keith Wilford^b, George D.W. Smith^a, Paul A.J. Bagot^a, Michael P. Moody^{a,*}

^a Department of Materials, University of Oxford, Parks Road, Oxford, OX1 3PH, United Kingdom

^b Rolls-Royce, PO Box 2000, SW1-70, Derby, DE21 7XX, United Kingdom

ARTICLE INFO

Article history:

Received 21 June 2016

Received in revised form

11 November 2016

Accepted 20 November 2016

Keywords:

17-4PH steel

Atom probe tomography

Cu-rich precipitates

α' (Cr-rich) phase

Precipitation hardening

ABSTRACT

A major concern for 17-4PH steels operating at elevated temperatures is embrittlement due to Fe-rich (α) and Cr-enriched (α') phase separation, along with precipitation of other detrimental phases. In this study the sequence of microstructural changes at the atomic scale in a 17-4PH steel is characterized by atom probe tomography (APT) at two different ageing temperatures, 480 °C and 590 °C. In the earliest stages of heat treatment at both temperatures, APT reveals that dislocations and matrix defects are highlighted by the segregation of NbN/CrN ionic species, providing heterogeneous nucleation sites for subsequent Cu-rich precipitates (CRPs) and Nb-rich precipitates, respectively. At the lower temperature, Cr-rich α' -phase also nucleates and ultimately a Mn, Ni, and Si-rich (MNS) phase was observed to form. The evolution in number density and fraction of CRPs and Cr-rich α' -phase, the latter of which was not observed at the higher temperature, has been quantified and their respective contributions to the overall precipitation hardening of the material has been estimated.

© 2016 Acta Materialia Inc. Published by Elsevier Ltd. This is an open access article under the CC BY license (<http://creativecommons.org/licenses/by/4.0/>).

1. Introduction

17-4PH is a precipitation hardened steel that normally contains 15.5–18.5 at.% Cr and 2.5–4.5 at.% Ni. After solution treatment (typically at 1038 °C) and quenching, it can be heat treated at different temperatures to develop a wide range of mechanical properties. Two typical heat treatment conditions are 482 °C for 1 h and 593 °C for 4 h. Treatment at 482 °C for 1 h gives the maximum hardness and strength, where 593 °C for 4 h improves toughness and ductility [1]. The resultant martensitic structure incorporating Cu-rich precipitates (CRPs) provides a good combination of mechanical properties and corrosion resistance, which makes it suitable for structural materials in nuclear and conventional power plants and other industries. However, few previous studies focused on atomic scale evolution of these materials at the precipitation hardening temperatures. Systematic characterisation of the sequence of precipitation is critical for understanding how the properties of the material evolve and how they can ultimately be optimised. The present research is focused on the microstructural

evolution at ageing temperatures 480 °C and 590 °C at different time scales.

Atom Probe Tomography (APT) is a unique microscopy technique that provides 3D reconstruction of microstructure at near atomic scale, making it suitable for analysis of the early stages of precipitation and phase separation. In particular, APT has previously been applied to the characterisation of α (Fe-rich)- α' (Cr-rich) phase separation, unambiguously detecting compositional variations and providing good contrast between phases [2,3], even when the precipitates are very small, i.e. 1–2 nm [4].

In 17-4PH, the formation of CRPs is considered to be the primary hardening mechanism, hence the development of this nanostructure has been intensively studied [5–8]. It is known that CRPs form by a BCC→9R→FCC phase transformation in ferritic/martensitic steels [9–11]. The previously coherent spherical CRPs were found to coarsen in size, become cylindrical in shape and segregate along grain boundaries or dislocations after prolonged ageing.

Binary Fe-Cr alloys are known to be susceptible to embrittlement when aged at intermediate temperatures in the range of 300–500 °C [12–15]. This effect, known as '475 °C embrittlement', is related to a microstructural evolution caused by redistribution of Cr. According to the phase diagram of the binary Fe-Cr system

* Corresponding author.

E-mail address: michael.moody@materials.ox.ac.uk (M.P. Moody).

[16–19], the Cr content in 17-4PH lies within the miscibility gap below 550 °C. There are two possible paths by which the microstructure can then evolve to reach the equilibrium state; nucleation and growth and spinodal decomposition. In 17-4PH, both nucleation growth and spinodal decomposition have been reported. Miller and Burke made a direct observation of Cr-rich α' precipitates in 17-4PH aged at 480 °C utilizing atom probe field ion microscopy (APFIM) [5]. They also reported that no α' -phase was present in samples aged at a higher temperature (635 °C). As the ageing temperature is lowered, the decomposition path tends to become spinodal [19]. At 590 °C the concentration of Cr is outside of the miscibility gap. At 480 °C however, it is within the miscibility gap. It is important to understand the Cr redistribution behavior at these two precipitation hardening temperatures. A quantitative understanding of the development of Cr-rich precipitates as well as the impact of precipitates on changes in mechanical property of this material remains an issue of great importance.

The present study is focused on using APT to provide detailed analysis of the sequence of precipitation at the atomic scale in different stages of ageing in 17-4PH. The steel was aged at two temperatures, 480 °C and 590 °C, respectively, for times up to 1000 h. The nucleation, growth and coarsening of precipitates at the various ageing stages has been characterized and correlated to results from Vickers hardness testing, linking microstructure to a key mechanical property.

2. Experimental

The as-received material was an 8mm diameter as-rolled rod of 17-4PH. The bulk chemical composition of the as-received sample and measured composition by APT analysis on a solution treated sample is shown in Table 1.

The material was sectioned into 15cm in lengths and solution treated at 1040 °C for 1 h and quenched in oil. Samples were then heat treated at 480 °C to 10 min, 30 min, 1 h, 2 h, 24 h, 120 h, 260 h, 360 h, 1000 h and 590 °C to 10 min, 20 min, 30 min, 2 h, 24 h respectively. There is an associated error of ± 4 °C in the actual temperature depending on the specimen's position in the furnace.

1mm thick disc samples for hardness and X-ray diffraction (XRD) testing were cut from the heat treated materials and then polished to colloidal silica finish. The Vickers hardness was obtained by averaging 10 randomly selected regions under a load of 30kg. Standard θ - 2θ X-ray diffraction patterns were obtained in a Philips PW1710 diffractometer using Cu K α radiation. The generator settings were 35 kV and 50 mA and the diffractograms were collected over a 2θ range of 35–120° with a step width of 0.02° and a counting time of 1 s/step.

The needle-shaped specimens required for APT were prepared by a standard two-stage electro-polishing method. In the first stage, the samples were polished using a 25 vol % perchloric/acetic acid solution at 12–16 V D.C. They were then polished to suitable sharpness using 2 vol % perchloric acid in 2-butoxyethanol solution at 4–6 V. APT analysis was carried out using a Cameca Local Electrode Atom Probe (LEAP) 3000X HR, with a 532 nm wavelength green laser. Initial APT experiments in voltage-pulsing mode revealed the specimens were prone to fracture, most likely due to

the presence of carbides. Hence subsequent specimens were analysed in laser-pulsing mode, using laser pulse energies of 0.4 nJ. The specimen temperature and pulse repetition rate were set to 50 K and 200 kHz, respectively. A more detailed discussion of APT theory, procedure and data analysis can be found in Refs. [20,21].

In the reconstructed APT data, the identification and characterization of CRPs was undertaken using the maximum separation method [22]. In simple terms, the distance separating a solute atom, identified as Cu, from its nearest solute neighbours is measured within the data. If this distance is less than a defined value, d_{\max} , the two solute atoms are considered to be part of the same cluster. This step is repeated for all the solute atoms in the data. Finally, a set of distinct solute clusters is defined by connecting all of the spatially associated atoms, regardless of chemical identity. Any cluster incorporating less than a defined number of atoms, N_{\min} , is removed from the analysis to remove contributions from very small clusters statistically likely to form randomly in the microstructure. In this study, the size distribution of the CRPs changed significantly with annealing time. Thus the chosen parameters to define the clusters were carefully adjusted for the APT analysis of each heat treatment condition. Too large a d_{\max} value can result in occasions where multiple discrete precipitates are identified as a single precipitates. Conversely, if the d_{\max} value is too small, a single large precipitate can be defined by the analysis as multiple smaller features. The parameters chosen to define the maximum separation were in the range of $d_{\max} = 1.0$ – 1.2 nm and $N_{\min} = 25$ atoms.

The Cr-rich α' phase and Mn, Ni, Si (MNS) rich phase were separated from the matrix using isoconcentration algorithms available within the CAMECA IVAS software. According to the Fe–Cr binary phase diagram, the concentration of Cr in the α' phase at equilibrium is higher than 90 at.%. Thus Cr is chosen as the clustering atom and a threshold value of Cr concentration 40 at.% was taken to identify Cr-rich phase. The threshold value is substantially higher than the matrix Cr composition to exclude any random compositional variations. For the MNS phase, the clustering atoms were chosen as Mn, Ni, Si and the isoconcentration surface was taken where the total concentration of Mn+Ni+Si equals 50 at.%.

The number density, N , of clusters identified within the reconstruction was calculated using the following formula:

$$N = \frac{n\eta}{N_{\text{tot}}\Omega} \quad (1)$$

where n is the total number of clusters in the analysed volume, N_{tot} is the total number of atoms in the reconstruction, Ω is the volume of one solute atom, taken as $1.178 \times 10^{-2} \text{ nm}^3$, assuming the solutes have a similar volume as Fe, while η is the detection efficiency of the LEAP 3000X HR, estimated to be 0.37 in the case of a reflectron-equipped instrument.

The corresponding cluster volume fraction, f , is estimated by:

$$f = \frac{\sum_{i=1}^n N_{\text{sol}}}{N_{\text{tot}}} \quad (2)$$

where N_{sol} is the number of solutes (i.e. Cu) in a precipitate and N_{tot} is the total number of atoms in the sample.

Table 1

Concentrations of the main elements of as-received 17-4PH and measured concentrations by APT (at.%). Errors are obtained from averaging results from 4 different samples.

Element	Fe	Cr	Ni	Cu	Mn	Si	Nb	Mo	Co	V	N	C
Bulk	74.20	16.42	4.41	2.90	0.75	0.67	0.15	0.08	0.06	0.05	0.12	0.06
APT	74.15	16.90	4.45	2.51	0.73	0.69	0.09	0.06	0.07	0.06	0.16	0.09
Error (\pm)	1.01	0.41	0.39	0.23	0.01	0.02	0.01	0.02	0.01	0.01	0.11	0.05

The radius (r) of a precipitate was equated to that of the volume equivalent sphere:

$$r = \sqrt[3]{\frac{3N_{\text{tot}}\Omega}{4\pi\eta}} \quad (3)$$

There is a possibility with this approach of under-estimating the size and volume fraction of solutes because the matrix atoms are excluded from the calculation. However, trajectory aberrations that affect the spatial resolution of reconstructed atoms in the region of the precipitates can cause an overestimation of matrix atoms to be associated to the precipitates. Furthermore, the APT measured composition of the dominant solute(s) in precipitates was very high: The Cr content in the Cr-rich α' phase exceeds 70 at.%; The Mn+Ni+Si content exceeds 80 at.% in the Mn, Ni, Si-rich (MNS) phase; and the Cu content in CRPs exceeds 50 at.%. Hence, the systematic method described above was deemed to be a reasonable approach for estimating the radius r and volume fraction f .

3. Results and discussion

3.1. Hardness variation

The variation in Vickers hardness of the specimens at both heat treatment temperatures as a function of holding time is shown in Fig. 1. The value at 0 h represents the hardness after solution treatment and oil quenching. The error is the standard deviation after averaging over 10 measurements. The hardness variation exhibits a dramatic difference between the two temperatures. At 480 °C, the hardness peaks around 1 h, higher than the initial value by ~145 (HV30). At later times, the hardness remains steady up to 360 h. A decreasing trend is only observed after the measurement at 1000 h. In contrast, at the higher temperature 590 °C, a sharp peak in hardness was observed after 10 min followed by a sharp drop. The peak hardness at 480 °C is higher than the peak hardness at 590 °C by ~40 (HV30).

3.2. Precipitation sequence

3.2.1. Solution treated microstructure

The XRD results from various stages of heat treatment are provided in the Supplementary document. After solution treatment at 1040 °C and oil quenching the XRD results showed a pure BCC lattice, indicating the formation of martensite. No precipitation or segregation is observed in the APT reconstruction after solution

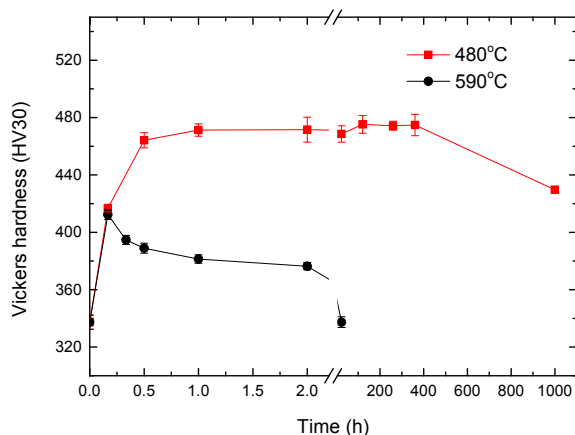


Fig. 1. Variations in hardness of the 17-4PH with heat treatment time at 480 °C and 590 °C.

treatment, with all the elements randomly distributed. Previous TEM studies have shown that at this solution treated stage, the microstructure is defined by a lath martensitic matrix having a high dislocation density and a low amount of carbide particles [7,8]. The absence of carbides observed throughout this study is most likely due to the relatively large distance between such features relative to the very small sampling volume of a typical APT analysis.

3.2.2. Heat treatment at 480 °C

At 480 °C up to 1000 h, XRD results showed a pure BCC structure, indicating that martensite is stable at this temperature. However from the APT results, after ageing for only 10 min the first change in the atomic scale chemical distribution can already be observed. The corresponding atom maps are shown in Fig. 2. In the APT experiment N is detected exclusively in the form of complex molecular ions, such as CrN^+ and NbN^+ . The interconnected structure displayed is possibly due to the migration of N to dislocations and matrix defects. All other elements appear homogeneously distributed.

After heat treatment for 2 h at 480 °C, segregation of NbN and CrN ions is apparent, as shown in Fig. 3a. Furthermore, a high number density of CRPs and Nb-rich precipitates are now observed to have formed. Fig. 3b is a close-up showing Ni and Mn co-segregation with Cu, which is attributed to the Ni and Mn reducing the interfacial energy [23–25]. From Fig. 3a, the Nb-rich precipitates are smaller in size than CRPs.

Fig. 3c is a 6nm thick vertical slice taken from the 3D reconstructed image in Fig. 3a, to highlight the spatial correlation between the observed precipitates and the NbN/CrN segregation. CRPs were observed to nucleate both in the matrix and also heterogeneously at crystal defects, the latter identified by the segregation of NbN/CrN ion, has been highlighted by the red dashed lines in Fig. 3c. The Nb-rich precipitates were found to form adjacent to CRPs in the matrix, a trend highlighted within the black dashed circles of Fig. 3c. The same phenomenon was also observed in all the other samples aged for longer times. The diffusion coefficient at 480 °C of Cu in α -iron is approximately $(5-6) \times 10^{-22} \text{ m}^2/\text{s}$ according to the equation proposed in Refs. [26,27], while for Nb in α -iron this is approximately $5.4 \times 10^{-23} \text{ m}^2/\text{s}$ [28], substantially lower than Cu. Thus, it is probable that the CRPs start to nucleate in the matrix prior to the Nb-rich precipitates. The solubility of Nb in Cu is low, so it will be rejected into the matrix as the CRPs grow. Furthermore, the solubility of Nb in matrix Fe is also low, and so it will enrich at the interface between CRPs and the matrix.

APT atom maps from the analysis after ageing for 120 h are shown in Fig. 4a. The CRPs have coarsened. Nb-rich precipitates are also still observed. In order to characterise the composition of the Nb-rich precipitates, the isoconcentration surface of Nb content at 2 at.% is chosen to separate the precipitates from the matrix. The measured concentrations of major elements within the isoconcentration surface are listed as a function of ageing time in Table 2. In the beginning (2–120 h), the precipitates contains about 10 at.% Nb. The Ni content in the precipitates reaches higher as the ageing time increases. Cr is also enriched by 1–4 at.% in the precipitates. The enrichment factor of Nb compared to the matrix Nb content was the largest for any element. After 260 h, the Nb concentration in the precipitates decreased as did the levels of Fe and Cr. A significant enrichment of Si and Mn was found in the precipitates. After 360 h, Ni, Mn and Si become the dominant elements in the precipitates, which will be discussed in detail in the following section.

In addition to the CRPs and Nb-rich precipitates, Cr-rich regions are also now observed after 120 h. Distinct Cr-rich regions can be seen in the 5nm thick Cr atom map slice in Fig. 4a. Isoconcentration surfaces for 40 at.% Cr are shown in Fig. 4b to highlight the Cr-rich

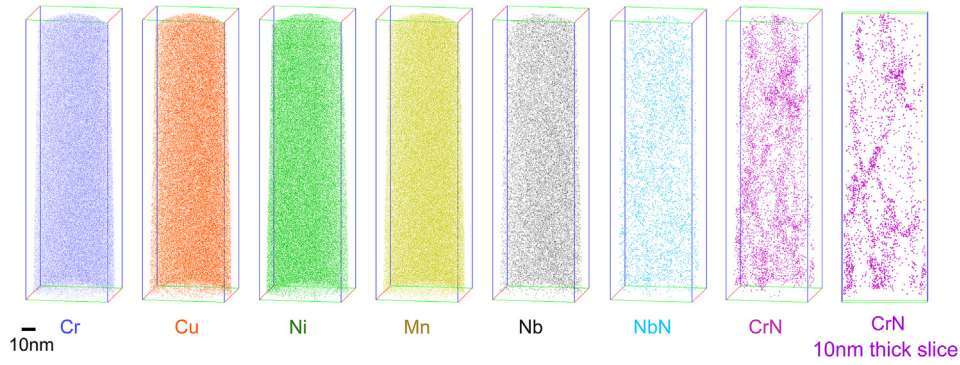


Fig. 2. Atom maps of 17-4PH heat treated for 10 min at 480 °C showing segregation of CrN, most likely to dislocations/other matrix defects.

regions, which are 1–3nm in size. A compositional proximity histogram (proxigram) indicating the chemical composition as a function of distance from the Cr-rich region/matrix interface, as defined by these isoconcentration surfaces is shown in Fig. 4c. The average Cr concentration at the core of Cr-rich particles is 70–80 at.%, somewhat lower than the estimated value from phase diagram of 90–95 at.% [29]. The reason for this under estimation of

Cr is most likely the well-known local magnification effect of APT [20,30,31]. Local magnification effects exist in many alloy systems. In Fe-Cr alloys, Cr has a lower evaporation field than Fe which results in a localised region of lower curvature at the surface of the specimen. The inability to account for this in the reconstruction algorithm causes an erroneous projection of matrix Fe into the precipitates, leading to a lower Cr-content to be measured inside

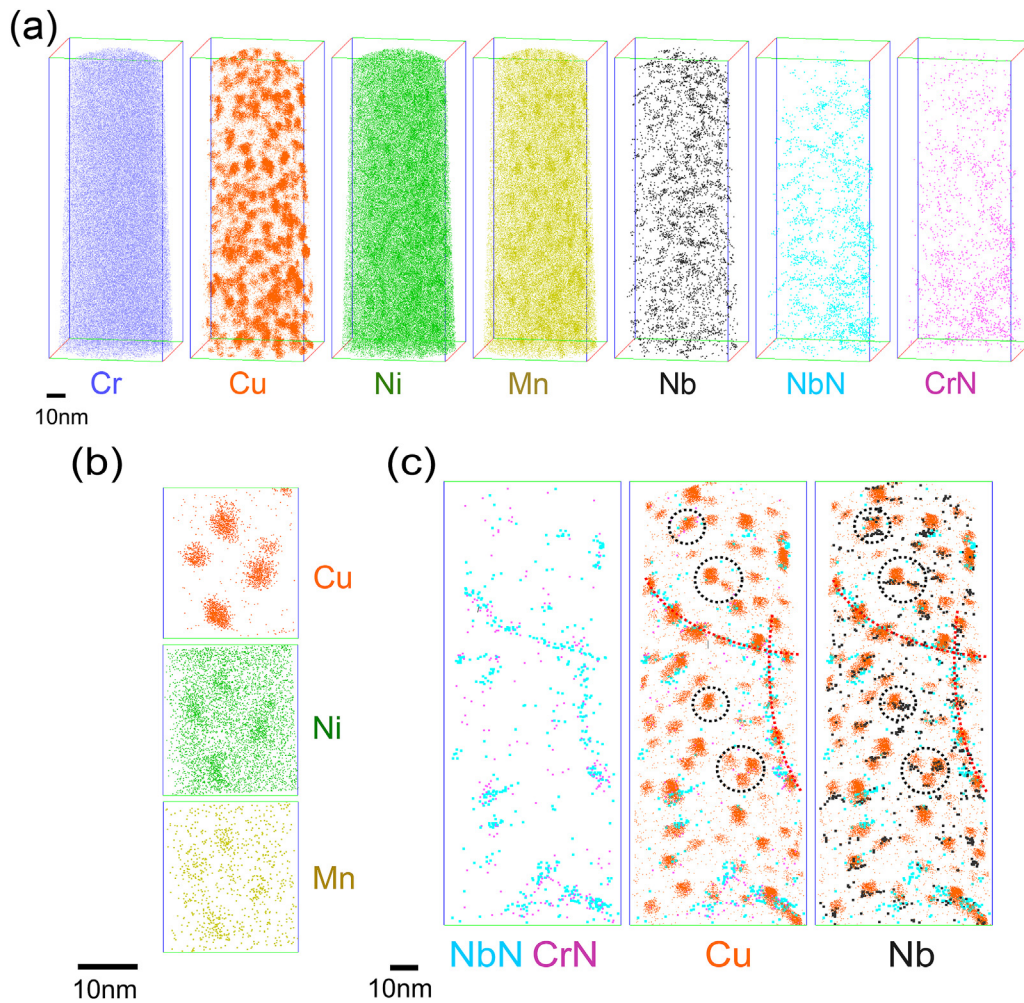


Fig. 3. (a) Atom maps of 17-4PH heat treated for 2 h at 480 °C; (b) 5nm-thick slice taken from the analysis, highlighting the co-segregation of Ni and Mn with Cu; (c) 6nm-thick slice close up view of segregation of CrN (pink), NbN (light blue), CRPs (orange) and Nb-rich precipitates (black) showing that CRPs are forming both at the defects (highlighted by red dashed line) and also in the matrix; Nb forms clusters adjacent to CRPs in the matrix (highlighted by black dashed line). (For interpretation of the references to colour in this figure legend, the reader is referred to the web version of this article.)

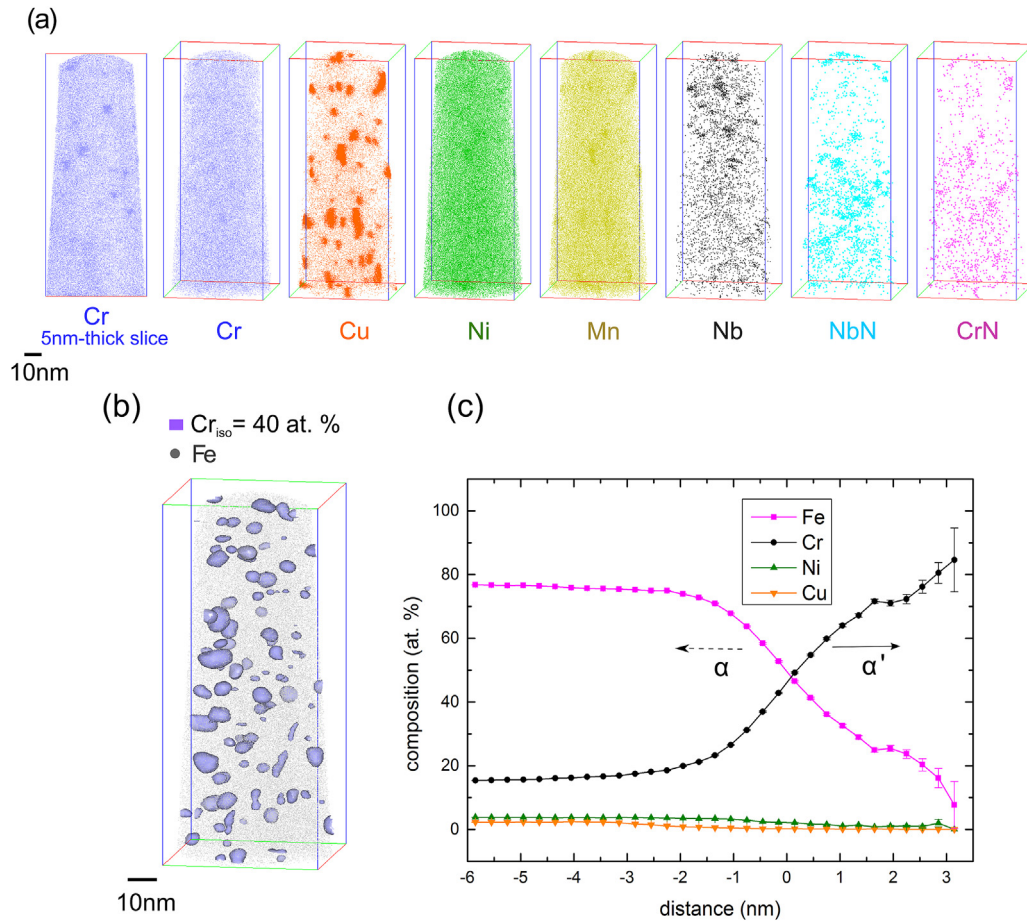


Fig. 4. (a) Atom maps of 17-4PH heat treated for 120 h at 480 °C showing the Cr rich α' precipitates along with other previously identified CRPs, Nb/Cr-nitrides; (b) Isoconcentration surfaces of 40 at.% Cr concentration. Grey dots represent 0.5% of total Fe atoms; (c) Concentration proxigram plotted from the isoconcentration-surfaces, indicating the average composition of the Cr-rich precipitates.

the precipitates. In irradiated Fe-Cr alloys, a lower Cr content has also been found by various APT measurements [32,33]. The second possibility could be a modification of the solubility limit by other alloying elements.

Most of the α' precipitates are next to CRPs and Nb-rich precipitates, or else along the regions of NbN and CrN segregation. This is more obvious at longer ageing times, and when a larger number of α' precipitates have formed. Fig. 5 shows two 5nm thick slices taken from the APT analysis of a specimen aged for 260 h. Here, the Cr rich region preferentially forms next to NbN rich regions (highlighted in red circles) and Nb and Cu precipitates (highlighted in black circles). In 3D, most of the Cr-rich precipitates have nucleated heterogeneously adjacent to previously existing precipitates.

By 260 h, according to Table 2, the composition of the initial Nb-rich precipitates changes progressively with time, the Nb

concentration falling and the Mn, Ni, and Si concentrations increasing to a level at which the particles are best described as MNS phase, rather than Nb-rich precipitates. The elemental distributions of Cu, Ni, Mn and Si within two slices of a sample aged for 260 h are shown in Fig. 6. Here, the Ni and Mn atoms are not only co-segregating with Cu, but also forming discrete MNS precipitates (highlighted with black arrows). In irradiated reactor pressure vessel (RPV) steels, a MNS dominating phase first appeared as a shell around Cu precipitates to form a core-shell structure. With further ageing, discrete MNS dominant features grew as an appendage to the CRPs, thus the CRPs were considered to act as nucleants for the formation of MNS precipitates [34,35]. Most of the previous observation of such MNS phases were associated with CRPs [7]. Styman et al. [36] also reported the existence of MNS phases at grain boundaries in a long-term thermally aged RPV steel.

In the present study, the majority of the MNS phase was

Table 2
Concentration of the Nb-rich precipitates after different ageing times at 480 °C.

Ageing time (h)	Concentration (at.%)					
	Nb	Ni	Fe	Cr	Si	Mn
2	10.8 ± 1.0	10.4 ± 1.0	42.7 ± 1.9	20.0 ± 1.6	3.6 ± 1.0	0.9 ± 0.4
24	9.5 ± 0.5	12.1 ± 1.6	56.5 ± 2.4	16.5 ± 1.7	3.1 ± 0.9	0.2 ± 0.2
120	9.5 ± 0.5	17.1 ± 0.9	36.3 ± 1.1	20.2 ± 1.0	6.9 ± 0.6	1.4 ± 0.3
260	7.8 ± 0.1	29.8 ± 0.3	26.0 ± 0.2	14.5 ± 0.2	12.1 ± 0.2	3.9 ± 0.1
360	4.8 ± 0.1	44.9 ± 0.2	9.9 ± 0.1	7.3 ± 0.9	18.4 ± 0.1	10.2 ± 0.1

● Iso surface of Cr at 50 at.%

- Nb ● Cu ● NbN

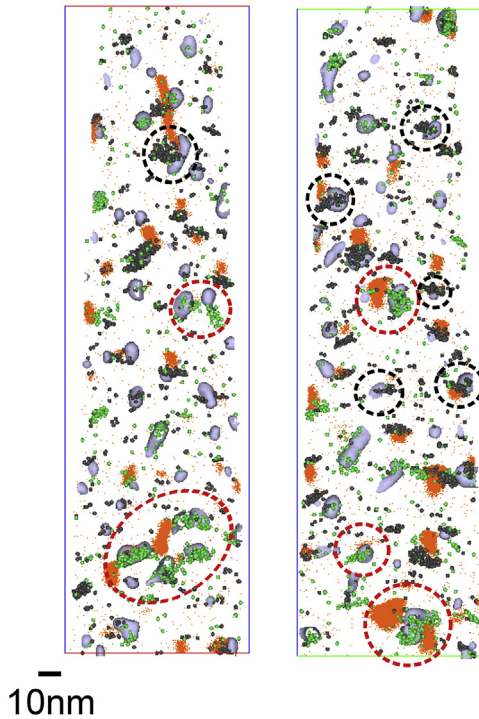


Fig. 5. 5nm slice taken from sample aged for 260 h at 480 °C, showing the heterogeneous nucleation of Cr-rich α' phase (light blue surfaces). (For interpretation of the references to colour in this figure legend, the reader is referred to the web version of this article.)

observed to precipitate attached to the CRPs, but not all. Furthermore, as discussed above, the CRPs, Nb-rich precipitates and Cr-rich precipitates all nucleate in close proximity to each other. Thus it is difficult to confirm which of these types of precipitates is primarily responsible for the heterogeneous precipitation of MNS phase or if there are synergistic effects. To investigate this further, examples of close-ups of isoconcentration surfaces where the concentration of Mn+Ni+Si at 50% (green surfaces), as well as the elemental distribution in the immediate area surrounding these phases are presented in Fig. 7a. This highlights that every MNS enriched precipitate in the APT reconstruction is also enriched in Nb. Two compositional proximity histograms of the precipitates (Isosurface1 and Isosurface2) are shown in Fig. 7b. From this concentration profile, the precipitates are seen to be enriched in Mn, Ni, Si and Nb. Hence in 17-4PH, it is proposed that Nb-rich precipitates have a dominant effect on formation of MNS phase. This can be further confirmed by the first nearest neighbour (1NN) distribution [37] of Ni and Nb as a function of time, as shown in Fig. 8. Similar Nb-Mn and Nb-Si nearest neighbour distance distributions were also found. Fig. 8 indicates clustering of Nb-Ni at 260 h and 360 h, when the MNS phase has been observed. At 2 h, there is some non-random distribution of Nb-Ni nearest neighbour distances. This is possibly related to the co-segregation of Ni to CRPs, adjacent to the Nb-rich precipitates, as shown in Fig. 3b. Thus it is reasonable that some non-randomness should be observed in the Nb-Ni spatial distribution. A plausible formation process of the MNS phase is as follows: First, Nb-rich precipitates form next to CRPs. The Ni, Mn, Si content in the Nb-rich precipitates increases with ageing time and then the Nb-rich precipitates transform into MNS precipitates. Thus, these MNS precipitates also contain significant amount of Nb.

Between 260 h and 360 h of ageing, the MNS enriched phase developed very quickly, increasing to a much larger volume fraction, as shown in Fig. 9a. An isoconcentration surface of Mn, Ni, Si at 50 at.% and the associated compositional proximity histogram at 360 h is plotted in Fig. 9b and c. From Fig. 9c, a steady ratio between

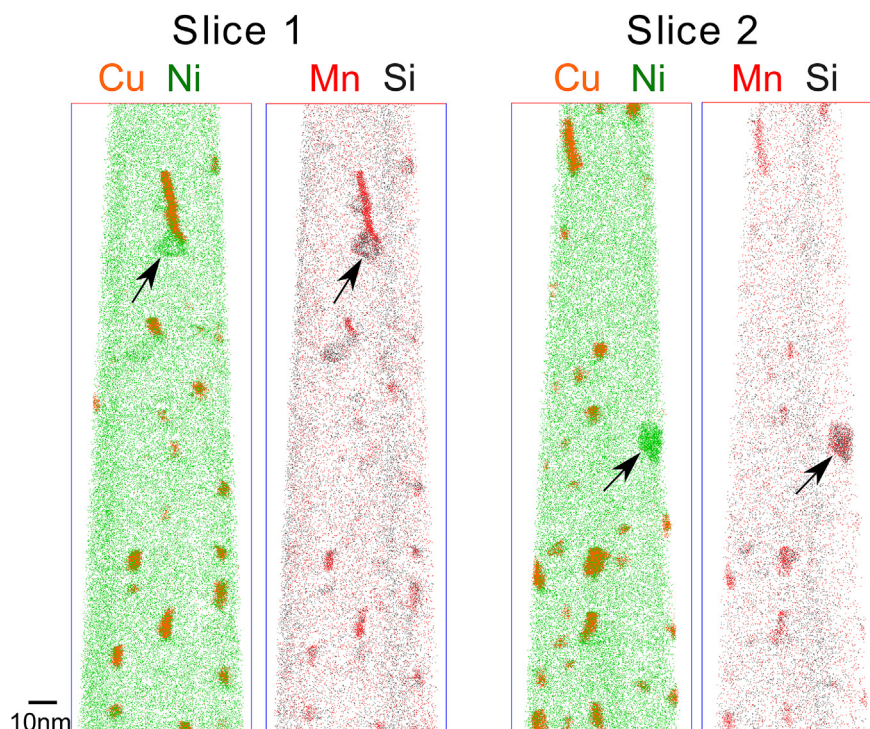


Fig. 6. Atom maps of Mn, Ni, Si and Cu showing the formation of Mn, Ni, Si enriched phase (arrowed) in a sample aged for 260 h at 480 °C. The thickness of the slice is 10nm.

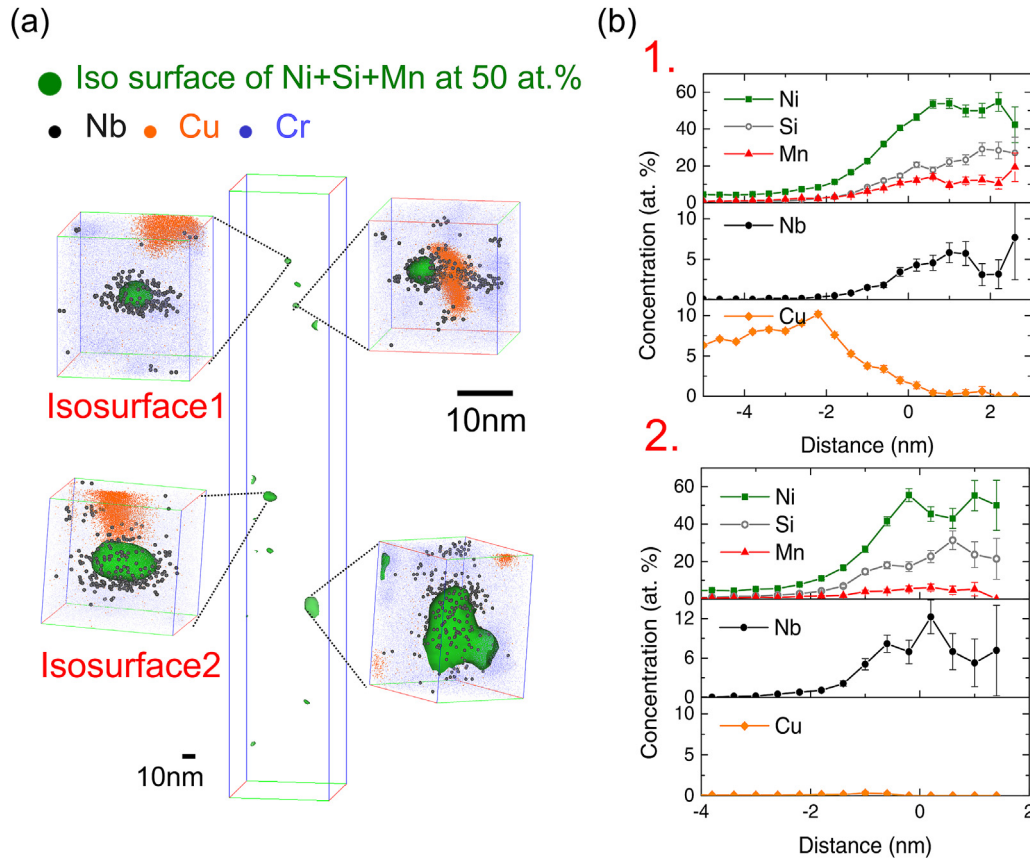


Fig. 7. (a) Isoconcentration surfaces of Mn+Ni+Si at 50 at.% and atom maps of Nb, Cu and Cr close to these regions in a sample aged for 360 h at 480 °C; (b) Concentration profiles of two of the MNS rich precipitates (Isosurface1 and Isosurface2).

Mn:Ni:Si is apparent. The concentration of Mn, Ni, Si is consistent with the theoretical composition of G-phase ($\text{Mn}_6\text{Ni}_{16}\text{Si}_7$), as shown in Table 3. The Nb contents in the smaller MNS precipitates

are much higher, consistent with the result from 260 h ageing. In the large precipitates, i.e. from Fig. 9c, the Nb concentration inside the MNS phase is about 1 at.%, which is lower than the value obtained from smaller precipitates, but still substantially higher than that in the matrix. A possible explanation for this is that after MNS phase formation from a small Nb-rich precipitate, the MNS phase grows larger and the limited amount of Nb available can spread throughout the precipitate, resulting in a lower average Nb concentration in the precipitates.

The question of the thermodynamic stability of MNS precipitates in RPV steels has led to significant debate. Ngayam-Happy et al. [38], using density functional theory (DFT) and Monte Carlo simulations, found that the interaction energy between Ni and Mn is in fact repulsive, and hence rejected the existence of this phase thermodynamically. Bonney et al. [39] used similar methods and concluded that even though the DFT calculation did result in a repulsive interaction between Ni-Mn pairs or triples, larger clusters can be kept together by an attractive binding energy. The presence of Cu was found to extend the temperature range of thermodynamic stability of the precipitates further. A more recent study has predicted that the MNS precipitates can be thermodynamically stable themselves without the presence of Cu under thermal ageing based on CALPHAD modelling [40]. In the current 17-4 PH steel, the Ni and Cu content is much higher than that of RPV steels. Thus it is plausible that MNS precipitates are thermodynamically stable at 480 °C, even though this is a much higher temperature compared to the studies of RPV steels.

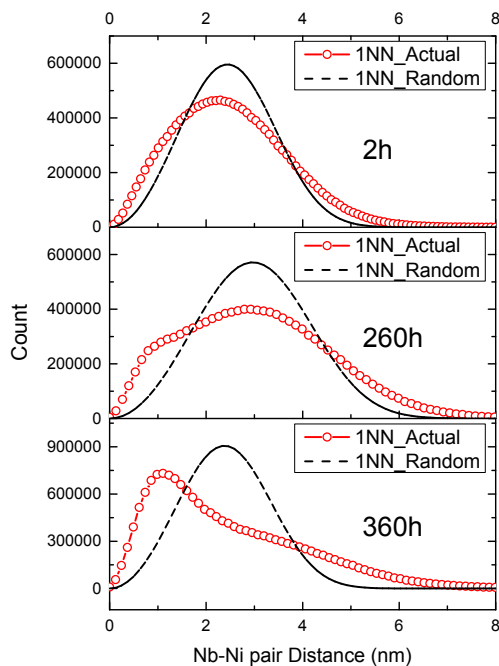


Fig. 8. First Nb–Ni nearest-neighbour distance distributions in 17-4PH aged at 480 °C for different heat treatment times.

3.2.3. Heat treatment at 590 °C

The XRD results indicate the existence of a pure BCC structure

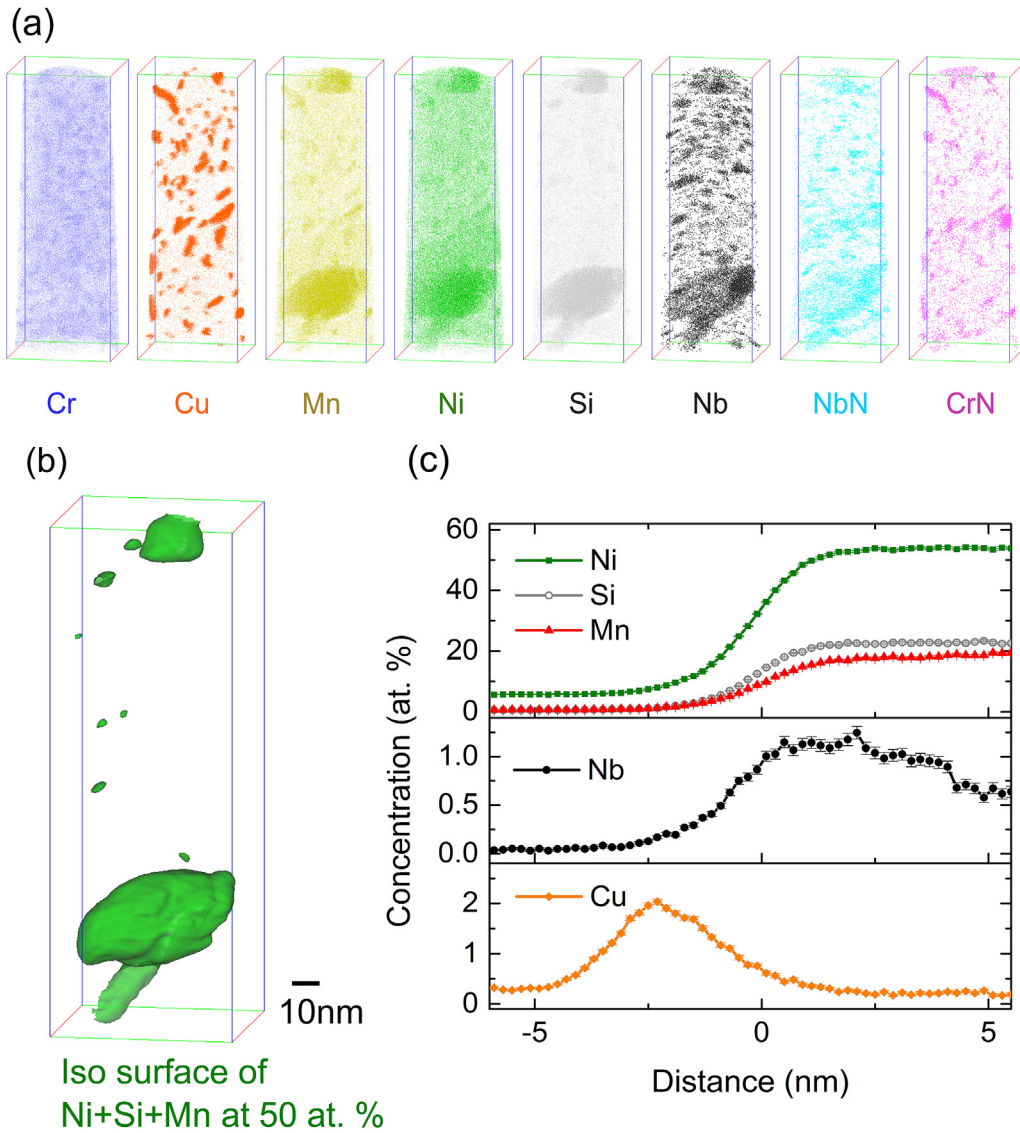


Fig. 9. (a) Atom maps of 17-4PH heat treated for 360 h at 480 °C; (b) Isoconcentration-surface at composition of Mn+Ni+Si at 50 at.% after 360 h; (c) Concentration proxigram of the larger precipitates at the bottom of analysis.

up to 2 h of heat treatment at 590 °C. After 24 h, 25% volume fraction of austenite is estimated to have formed.

APT analysis revealed that, heat treatment at 590 °C for only 20min is sufficient to produce CRPs, Nb-rich precipitates and NbN/CrN precipitates, as shown in Fig. 10a. One can observe that at this temperature, the distribution of CRPs is less homogeneous than at 480 °C. Fig. 10b shows a 6nm slice taken from the same analysis. It can be seen that the majority of the CRPs and Nb-rich precipitates are found along regions of NbN segregation and precipitation. This suggests that in this case the main process is heterogeneous nucleation at dislocations and other matrix defects. At higher temperature, the migration of solutes is accelerated, meaning

solutes can more easily diffuse to favorable nucleation sites. Also, from nucleation theory, the nucleation barrier for heterogeneous nucleation is smaller than that of homogeneous nucleation, making heterogeneous nucleation more favorable.

Fig. 11 shows the elemental distribution after 24 h at 590 °C. The CRPs have now coarsened to larger sizes, i.e. several tens of nm. However, no Cr-rich precipitates were present at this temperature. From the Fe-Cr phase diagram, the Cr content is within the solubility limit at 590 °C (863 K), which can explain the absence of Cr-rich precipitates.

3.3. Evolution of precipitates - volume fraction, number density and mean radius of precipitates at both temperatures

The number density, volume fraction and mean radius of the CRPs and Cr-rich precipitates were quantified using the methods described in the “Experimental” section. Fig. 12 shows the development of CRPs and Cr-rich precipitates in terms of number density (N) and average radius ($\langle r \rangle$) as a function of time at both temperatures. The error of the number density is the standard error

Table 3
Compositions of MNS enriched phase from APT data and G-phase ($Mn_6Ni_{16}Si_7$).

Elements	G-phase (at.%)	Our study (at.%)
Mn	21	17–20
Ni	55	53–55
Si	24	22–24

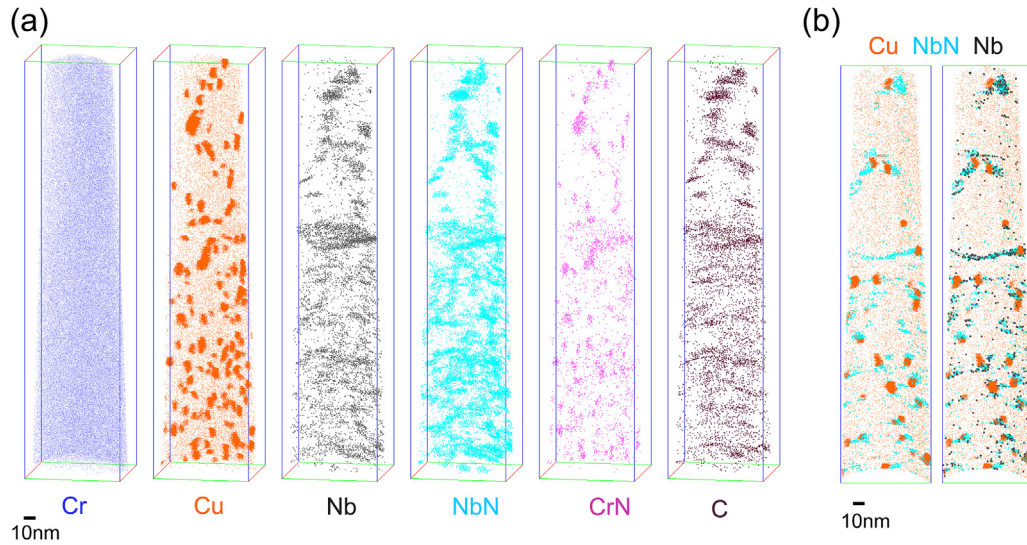


Fig. 10. (a) Atom maps of 17-4PH heat treated for 20 min at 590 °C; (b) 6nm-thick slice taken from the analysis, highlighting segregation of Cu and Nb at the NbN segregation (indicating dislocation and matrix defects).

after averaging the number density obtained from different cluster searching parameters. The error of the mean radius is the standard error after averaging the size of each precipitate population. Table 4 lists the volume fraction of the CRPs (f_{Cu}) and Cr-rich precipitates (f_{Cr}) across all ageing times/temperatures. The C_{Cu} and C_{Cr} is the overall concentration of Cu or Cr in the analysed volume.

- CRPs

According to Fig. 12, at both temperatures the number density of CRPs increases at the early stage of heat treatment then decreases strongly with annealing time. This is offset by a continuous growth of the average precipitate radius throughout the annealing time. Table 4 indicates that the change in the volume fraction of CRPs (f_{Cu}) is quite small after the precipitates form. It can be noted that even the slight fluctuation of volume fraction is actually related to the difference in the overall Cu concentration (C_{Cu}) within different micro-volumes sampled by the APT experiment. Thus we assume that CRPs have reached a maximum number density and volume fraction within 30 min at 480 °C or 10 min at 590 °C. Then the

existing smaller CRPs coarsen upon prolonged ageing, leading to a decrease in number density. Also the peak number density at 480 °C is much higher and the growth is much slower than that at 590 °C.

- Cr-rich precipitates

According to Fig. 12, at 480 °C the number density of Cr-rich precipitates starts to increase after 24 h, reaching a peak number density at about 120 h before dropping. Throughout this time the volume fraction and the mean radius of precipitates continuously increase. The process can be described as: 24–120 h is the initial nucleation and growth stage, during which more precipitates form but at the same time solutes also migrate to existing precipitates, thus increasing their size. From 260 to 1000 h, the number density decreases while the volume fraction and mean radius of precipitates increase, indicated a growth and coarsening stage free of further nucleation but with more solutes precipitating out from the matrix to existing precipitates.

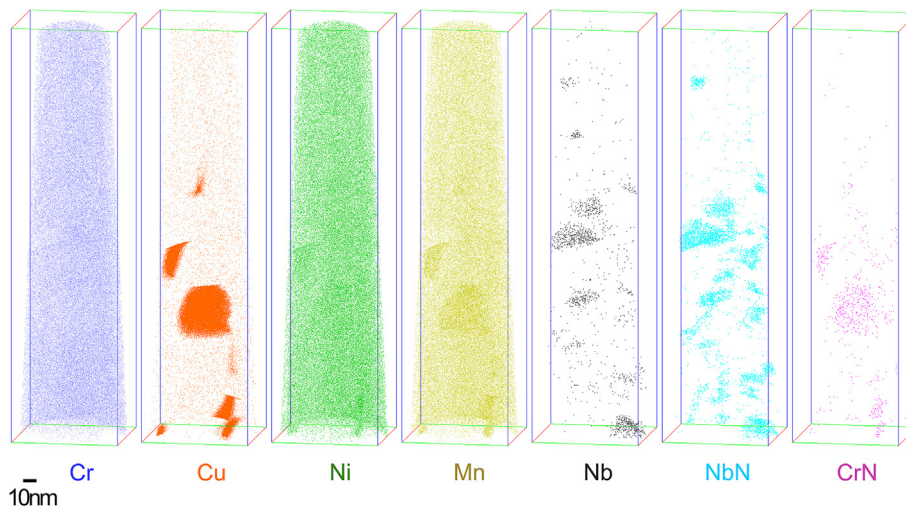


Fig. 11. Atom maps of 17-4PH heat treated for 24 h at 590 °C.

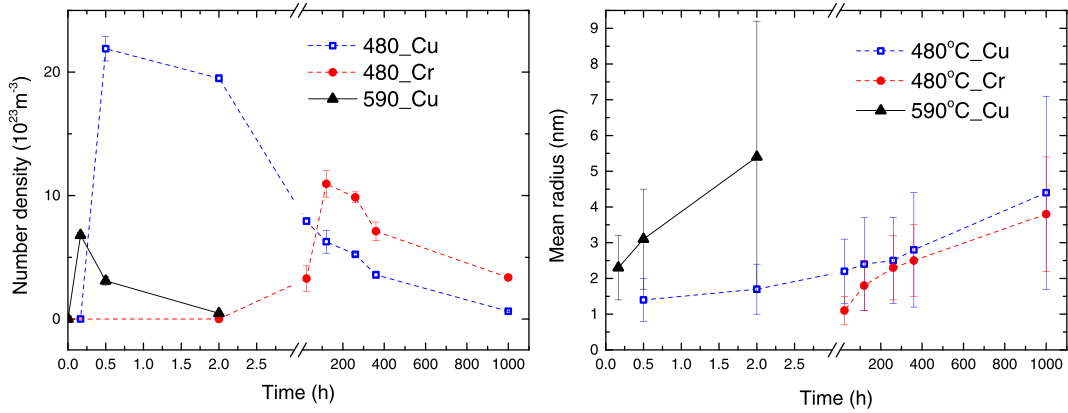


Fig. 12. Number density and mean radius of CRPs and Cr-rich precipitates.

3.4. Precipitation hardening effects

Upon thermal ageing of 17-4PH steels, CRPs, Nb-rich precipitates, Cr-rich precipitates and MNS precipitates have been observed. Nucleation of these features are thought to increase the hardness. The number density of MNS precipitates are much lower and the size of MNS precipitates are much larger compared to other precipitates. Thus their effect on hardness is negligible. The CRPs and Cr-rich precipitates are considered to be the main hardening precipitates. An estimation of the effect of CRPs and Cr-rich precipitates on yield strength is provided here and compared with the experimental yield strength increase obtained from Vickers hardness.

- Contribution of CRPs to hardness

It is known that the CRPs are attractive particles for dislocations with a smaller modulus compared to the matrix, thus the Russell-Brown model is appropriate to estimate the strengthening contribution of CRPs. From the difference in the modulus between CRPs and matrix, the increase in shear strength can be calculated by Refs. [41–43]:

$$\Delta\tau(\text{Cu}) = \frac{\alpha G b \sqrt{f_{\text{Cu}}}}{1.77 \langle r \rangle} \quad (4)$$

where α represents the strength of precipitates, G is the shear modulus of the matrix (83GPa from Ref. [41]), and b is Burgers vector (0.25nm for iron). For precipitates within a radius of 0.6nm–10nm, α varies between 0.2 and 0.4 [41,42]. Here, a common value 0.2 is used. Smaller precipitates represent weaker obstacles. Thus there will be an over-estimation of the effects of smaller precipitates and under-estimation of larger precipitates. The volume fraction, f , and the mean radius, $\langle r \rangle$, are those obtained from APT and presented in Table 4.

After solution treatment, Cu atoms are supersaturated in the

matrix. Upon thermal ageing, nearly all of the Cu becomes incorporated into precipitates. Hence, the solute solution strengthening contribution from Cu after 30 min should be negligible. The final expression of estimated increase in yield strength due to CRPs is then:

$$\Delta\sigma(\text{Cu}) = T\Delta\tau(\text{Cu}) - \sigma_{\text{Cu}}^0 = T \frac{\alpha G b \sqrt{f_{\text{Cu}}}}{1.77 \langle r \rangle} - \sigma_{\text{Cu}}^0 \quad (5)$$

where T is the Taylor factor, (2.5), σ_{Cu}^0 refers to the Cu solute solution strengthening at solution treatment condition, estimated to be 30MPa according to [44]. From Equation (4), the yield strength increase is proportional to the square root of the volume fraction and varies inversely with the mean precipitates radius. From Table 4, the volume fraction of CRPs is steady after their formation, but the mean radius increases with ageing time. The effect of CRPs on hardening should therefore be a monotonic decrease, which is not consistent with the observed steady hardness as a function of treatment time at 480 °C in Fig. 1.

- Contribution of Cr-rich precipitates on hardness

Compared to the CRPs, the shear modulus of Cr-rich precipitates is higher than that of the Fe-rich matrix, thus the dislocation interaction is repulsive. The atomistic simulation developed by Terentyev et al. [45] suggests that Cr-rich precipitates will be sheared and not bypassed. It is proposed that the increase in strength can be determined from the sum of modulus misfit strengthening (MMS) and chemical strengthening (CS). Firstly we consider the MMS model. Since the Cr-rich precipitates are of higher shear modulus, the Russell-Brown type model does not apply. Instead an expression previously utilised in Refs. [45,46] is employed, derived from a regular array of precipitates:

Table 4

Volume fraction of CRPs and Cr-rich precipitates. f_{Cu} and f_{Cr} is the volume fraction of CRPs and Cr-rich precipitates. C_{Cu} and C_{Cr} is the overall concentration of Cu and Cr in the sample.

Time	480 °C							590 °C		
	30 min	2 h	24 h	120 h	260 h	360 h	1000 h	10 min	20 min	24 h
f_{Cu} (at.%)	2.48±0.03	2.34±0.01	2.07±0.01	2.39±0.06	2.34±0.00	2.39±0.01	1.83±0.00	1.89±0.01	2.06±0.01	2.72±0.00
C_{Cu} (at.%)	2.53	2.35	2.08	2.39	2.35	2.40	1.84	1.93	2.19	2.93
f_{Cr} (at.%)	–	–	0.13±0.06	1.38±0.22	2.83±0.31	2.43±0.24	4.33±0.26	–	–	–
C_{Cr} (at.%)	16.6	16.8	16.9	16.8	16.6	15.8	17.0	16.8	16.7	17.0

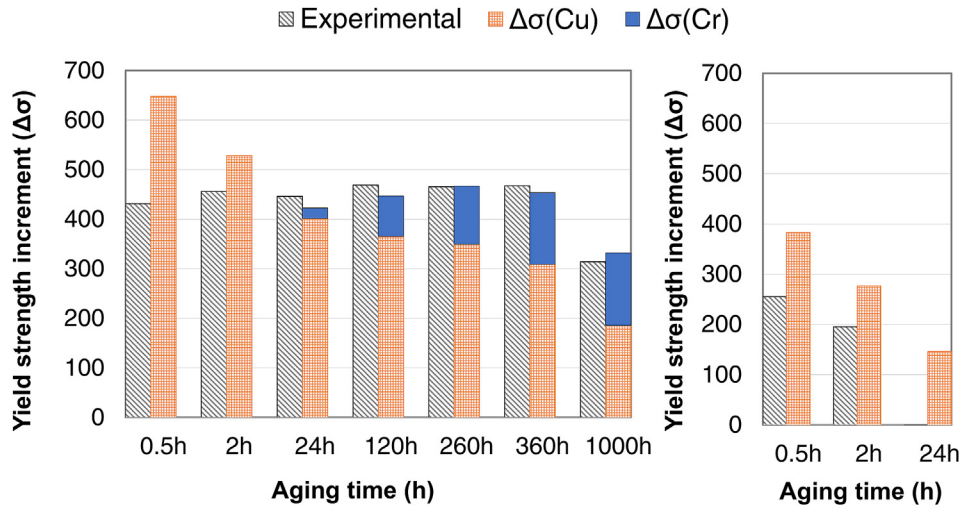


Fig. 13. Comparison between yield strength increases derived from hardness (black diagonal) and theoretical increase due to CRPs (orange grid) and Cr-rich precipitates (blue solid). (For interpretation of the references to colour in this figure legend, the reader is referred to the web version of this article.)

$$\Delta\tau_{MMS}(\text{Cr}) = \frac{\Delta G}{4\pi^2} \left(\frac{3\Delta G}{Gb} \right) [0.8 - 0.143 \ln(\langle r \rangle / b)]^{3/2} r^{1/2} f^{1/2} \quad (6)$$

where ΔG is the difference of modulus between Fe and Cr which was taken to be 33GPa [45]. Next we consider the CS model. The yield stress increment due to the surface area increase when a dislocation passes through a coherent precipitate can be obtained from Ref. [46]:

$$\Delta\tau_{CS}(\text{Cr}) = 2(3/\pi)^{1/2} G(\sigma_s/Gb)^{3/2} (b/\langle r \rangle)^{1/2} f^{1/2} \quad (7)$$

where σ_s is the energy per surface area, which was taken as 0.4 according to Schwen et al. [47]. Considering the relation of yield strength and shear stress, the increase in yield strength from Cr is then:

$$\Delta\tau(\text{Cr}) = T[\Delta\tau_{MMS}(\text{Cr}) + \Delta\tau_{CS}(\text{Cr})] \quad (8)$$

A comparison between the estimated theoretical strength increase and experimental measured strengthening from CRPs and Cr-rich precipitates is presented in Fig. 13. The experimental strength increase is obtained from the relationship between strength and hardness [48]. It should be noted that the interactions between different precipitates have not been considered here. Thus the figure should be treated as an illustration of the counterbalancing effects from CRPs and Cr-rich precipitates. The number should be taken as an estimate. From Fig. 13 at 480 °C, the calculated hardening effects of CRPs decrease with ageing time throughout the ageing time. This is related to the continuous coarsening of CRPs. The hardening from Cr-rich precipitates contributes significantly to the overall strength after 24 h and this continues to increase up to the longest characterised annealing time of 1000 h. Notably the contribution from Cr-rich precipitates compensates for the decrease in strength arising from the coarsening of the CRPs. It is proposed that this counterbalancing effects explain the steady hardness curve observed for precipitation hardening at 480 °C up to 360 h. At 1000 h, the estimated contributions from CRPs and Cr-rich precipitates were effectively comparable.

At 590 °C, there is no strengthening from Cr-rich precipitates. Consistent with experimental results, the estimated strengthening

from CRPs showed a monotonic decrease with ageing time. However, the estimated strength is higher than the experimental value. The most plausible reason for this is that at 590 °C, partial reversion to austenite occurs according to the XRD results. The hardness of austenite is substantially lower than that of martensite [49]. Also at higher temperature, matrix grain growth is faster than at lower temperature. Dislocations can be removed faster at higher annealing temperature. Thus, a softening of the matrix is expected, which is not considered in the current calculation of the precipitation hardening.

4. Conclusion

In this study, a 17-4PH steel was heat treated at two precipitation hardening temperatures (480 °C and 590 °C). Atom probe tomography has offered insights into the precipitation sequence in this steel. The following conclusions can be drawn:

- At 480 °C, the precipitation sequence can be summarized as: segregation of CrN/NbN to dislocation and matrix defects → CRPs and Nb-rich precipitates → Cr-rich precipitates → MNS phase.
- The initially nucleated precipitates act as favoured sites for heterogeneous nucleation of subsequent phases. MNS phase precipitates were transformed from Nb-rich precipitates.
- At 590 °C, no Cr-rich precipitates or MNS phase were present, consistent with the prediction from the phase diagram.
- The development of CRPs and Cr-rich precipitates (at 480 °C) in terms of number density, volume fraction has been characterized. The CRPs were in a growth and coarsening stage for most of the conditions examined. However an increase in number density and volume fraction of Cr-rich precipitates indicated a nucleation stage was also observed from 24 to 120 h at 480 °C.
- The hardening from CRPs was estimated to decrease at both temperatures as a function of ageing time due to over-ageing. However at 480 °C, the increasing contribution from Cr-rich precipitates largely compensate for the decreasing contribution from CRPs.

Acknowledgements

The authors would like to acknowledge the sponsorship

provided by the Chinese scholarship Council, materials and support provided by Rolls-Royce plc and the MFFP EPSRC Programme grant EP/H018921/1.

Appendix A. Supplementary data

Supplementary data related to this article can be found at <http://dx.doi.org/10.1016/j.actamat.2016.11.052>.

References

- [1] W. Do Yoo, J.H. Lee, K.T. Youn, Y.M. Rhyim, Study on the microstructure and mechanical properties of 17-4 PH stainless steel depending on heat treatment and aging time, *Solid State Phenom.* 118 (2006) 15–20.
- [2] M.K. Miller, J.M. Hyde, M.G. Hetherington, A. Cerezo, G.D.W. Smith, C.M. Elliott, Spinodal decomposition in Fe–Cr alloys: experimental study at the atomic level and comparison with computer models—I. Introduction and methodology, *Acta Metall. Mater.* 43 (1995) 3385–3401.
- [3] J.M. Hyde, M.K. Miller, M.G. Hetherington, A. Cerezo, G.D.W. Smith, C.M. Elliott, Spinodal decomposition in Fe–Cr alloys: experimental study at the atomic level and comparison with computer models—II. Development of domain size and composition amplitude, *Acta Metall. Mater.* 43 (1995) 3403–3413.
- [4] M. Bachhav, G. Robert Odette, E.A. Marquis, α' precipitation in neutron-irradiated Fe–Cr alloys, *Scr. Mater.* 74 (2014) 48–51.
- [5] M.K. Miller, M.G. Burke, Characterization of copper precipitation in a 17/4 PH steel: a combined APFIM/TEM study, in: *Proc. 5th Inter. Conf. Environ. Degrad. Mater. Nucl. Power Syst. React., LaGrange Park, IL, 1991*, pp. 689–695.
- [6] C.N. Hsiao, C.S. Chiou, J.R. Yang, Aging reactions in a 17-4 PH stainless steel, *Mater. Chem. Phys.* 74 (2002) 134–142.
- [7] M. Murayama, K. Hono, Y. Katayama, Microstructural evolution in a 17-4 PH stainless steel after aging at 400 °C, *Metall. Mater. Trans. A* 30 (1999) 345–353.
- [8] U.K. Viswanathan, S. Banerjee, R. Krishnan, Effects of aging on the microstructure of 17-4 PH stainless steel, *Mater. Sci. Eng. A* 104 (1988) 181–189.
- [9] G.M. Worrall, J.T. Buswell, C.A. English, M.G. Hetherington, G.D.W. Smith, A study of the precipitation of copper particles in a ferrite matrix, *J. Nucl. Mater.* 148 (1987) 107–114.
- [10] P.J. Othen, M.L. Jenkins, G.D.W. Smith, High-resolution electron microscopy studies of the structure of Cu precipitates in α -Fe, *Philos. Mag.* A 70 (1994) 1–24.
- [11] H.R. Habibi Bajguirani, C. Servant, G. Cizeron, TEM investigation of precipitation phenomena occurring in PH 15-5 alloy, *Acta Metall. Mater.* 41 (1993) 1613–1623.
- [12] M.H. Mathon, Y. de Carlan, G. Geoffroy, X. Averty, A. Alamo, C. de Novion, A SANS investigation of the irradiation-enhanced α - α' phases separation in 7–12 Cr martensitic steels, *J. Nucl. Mater.* 312 (2003) 236–248.
- [13] S.S. Brenner, M.K. Miller, W.A. Soffa, Spinodal decomposition of iron-32 at.% chromium at 470°C, *Scr. Metall.* 16 (1982) 831–836.
- [14] J.C. LaSalle, L.H. Schwartz, Further studies of spinodal decomposition in Fe–Cr, *Acta Metall.* 34 (1986) 989–1000.
- [15] B. Yrieix, M. Guttman, Aging between 300 and 450°C of wrought martensitic 13–17 wt-%Cr stainless steels, *Mater. Sci. Technol.* 9 (1993).
- [16] T. Massalski, H. Okamoto, Fe–Cr Phase Diagram, in: *Bin. Alloy Phase Diagrams*, second ed., ASM International, Materials Park, Ohio, 1990, pp. 1271–1273.
- [17] J. Andersson, B. Sundman, Thermodynamic properties of the Cr–Fe system, *Calphad* 11 (1987) 83–92.
- [18] G. Bonny, D. Terentyev, L. Malerba, On the α - α' miscibility gap of Fe–Cr alloys, *Scr. Mater.* 59 (2008) 1193–1196.
- [19] J. Wang, H. Zou, C. Li, S. Qiu, B. Shen, The spinodal decomposition in 17-4PH stainless steel subjected to long-term aging at 350 °C, *Mater. Charact.* 59 (2008) 587–591.
- [20] B. Gault, M.P. Moody, J.M. Cairney, S.P. Ringer, *Atom Probe Microscopy*, Springer Science & Business Media, New York, 2012.
- [21] M.K. Miller, A. Cerezo, M.G. Hetherington, G.D.W. Smith, *Atom Probe Field Ion Microscopy*, Clarendon Press, Oxford, UK, 1996.
- [22] J. Hyde, C. English, An analysis of the structure of irradiation induced Cu-enriched clusters in low and high nickel welds, in: *MRS Proc.* 2000.
- [23] A. Seko, S.R. Nishitani, I. Tanaka, H. Adachi, E.F. Fujita, First-principles calculation on free energy of precipitate nucleation, *Calphad* 28 (2004) 173–176.
- [24] A. Seko, N. Odagaki, S.R. Nishitani, I. Tanaka, H. Adachi, Free-energy calculation of precipitate nucleation in an Fe–Cu–Ni alloy, *Mater. Trans.* 45 (2004) 1978–1981.
- [25] O.I. Gorbatov, Y.N. Gornostyrev, P.A. Korzhavyi, A.V. Ruban, Effect of Ni and Mn on the formation of Cu precipitates in α -Fe, *Scr. Mater.* 102 (2015) 11–14.
- [26] M.S. Anand, R.P. Agarwala, Diffusion of copper in iron, *J. Appl. Phys.* 37 (1966) 4248–4251.
- [27] G. Salje, M. Feller-Kniepmeier, The diffusion and solubility of copper in iron, *J. Appl. Phys.* 48 (1977) 1833–1839.
- [28] N. Oono, H. Nitta, Y. Iijima, Diffusion of niobium in ALPHA-iron, *Mater. Trans.* 44 (2003) 2078–2083.
- [29] L. Malerba, A. Caro, J. Wallenius, Multiscale modelling of radiation damage and phase transformations: the challenge of FeCr alloys, *J. Nucl. Mater.* 382 (2008) 112–125.
- [30] F. Vurpillot, A. Bostel, D. Blavette, Trajectory overlaps and local magnification in three-dimensional atom probe, *Appl. Phys. Lett.* 76 (2000) 3127.
- [31] M.K. Miller, M.G. Hetherington, Local magnification effects in the atom probe, *Surf. Sci.* 246 (1991) 442–449.
- [32] V. Kuksenko, C. Pareige, C. Genevois, P. Pareige, Characterisation of Cr, Si and P distribution at dislocations and grain-boundaries in neutron irradiated Fe–Cr model alloys of low purity, *J. Nucl. Mater.* 434 (2013) 49–55.
- [33] V. Kuksenko, C. Pareige, P. Pareige, Cr precipitation in neutron irradiated industrial purity Fe–Cr model alloys, *J. Nucl. Mater.* 432 (2013) 160–165.
- [34] C.L. Liu, G.R. Odette, B.D. Wirth, G.E. Lucas, A lattice Monte Carlo simulation of nanophase compositions and structures in irradiated pressure vessel Fe–Cu–Ni–Mn–Si steels, *Mater. Sci. Eng. A* 238 (1997) 202–209.
- [35] P.B. Wells, T. Yamamoto, B. Miller, T. Milot, J. Cole, Y. Wu, et al., Evolution of manganese–nickel–silicon-dominated phases in highly irradiated reactor pressure vessel steels, *Acta Mater.* 80 (2014) 205–219.
- [36] P.D. Styman, J.M. Hyde, K. Wilford, A. Morley, G.D.W. Smith, Precipitation in long term thermally aged high copper, high nickel model RPV steel welds, *Prog. Nucl. Energy* 57 (2012) 86–92.
- [37] J.M. Cairney, K. Rajan, D. Haley, B. Gault, P.A.J. Bagot, P.-P. Choi, et al., Mining information from atom probe data, *Ultramicroscopy* 159 (2015) 324–337.
- [38] R. Ngayam-Happy, C.S. Becquart, C. Domain, L. Malerba, Formation and evolution of MnNi clusters in neutron irradiated dilute Fe alloys modelled by a first principle-based AKMC method, *J. Nucl. Mater.* 426 (2012) 198–207.
- [39] G. Bonny, D. Terentyev, A. Bakaev, E.E. Zhurkin, M. Hou, D. Van Neck, et al., On the thermal stability of late blooming phases in reactor pressure vessel steels: an atomistic study, *J. Nucl. Mater.* 442 (2013) 282–291.
- [40] W. Xiong, H. Ke, R. Krishnamurthy, P. Wells, L. Barnard, G.R. Odette, et al., Thermodynamic models of low-temperature Mn–Ni–Si precipitation in reactor pressure vessel steels, *MRS Commun.* (2014) 1–5.
- [41] K.C. Russell, L.M. Brown, A dispersion strengthening model based on differing elastic moduli applied to the iron-copper system, *Acta Metall.* 20 (1972) 969–974.
- [42] K. Nogiwa, N. Nita, H. Matsui, Quantitative analysis of the dependence of hardening on copper precipitate diameter and density in Fe–Cu alloys, *J. Nucl. Mater.* 367–370 (2007) 392–398.
- [43] K. Fujii, K. Fukuya, R. Kasada, A. Kimura, T. Ohkubo, Effects of tensile stress on Cu clustering in irradiated Fe–Cu alloy, *J. Nucl. Mater.* 458 (2015) 281–287.
- [44] J. Syarif, K. Nakashima, T. Tsuchiyama, S. Takaki, Effect of solute copper on yield strength in dislocation-strengthened steels, *ISIJ Int.* 47 (2007) 340–345.
- [45] D.A. Terentyev, G. Bonny, L. Malerba, Strengthening due to coherent Cr precipitates in Fe–Cr alloys: atomistic simulations and theoretical models, *Acta Mater.* 56 (2008) 3229–3235.
- [46] J.W. Martin, *Micromechanisms in Particle-Hardened Alloys*, Cambridge University Press, Cambridge, UK, 1980.
- [47] D. Schwen, E. Martinez, A. Caro, On the analytic calculation of critical size for alpha prime precipitation in FeCr, *J. Nucl. Mater.* 439 (2013) 180–184.
- [48] B. Yrieix, M. Guttman, Aging between 300 and 450°C of wrought martensitic 13–17 wt-%Cr stainless steels, *Mater. Sci. Technol.* 9 (1993) 125–137.
- [49] G. Krauss, Martensite in steel: strength and structure, *Mater. Sci. Eng. A* 273–275 (1999) 40–57.